Low-Cost Depth and Radiological Sensor Fusion to Detect Moving Sources

Phillip Riley
University of Florida
Gainesville, Fl
philllipriley.ufl.edu

Andreas Enqvist
University of Florida
Gainesville, Fl
enqvist@mse.ufl.edu

Sanjeev J. Koppal
University of Florida
Gainesville, Fl
sjkoppal@ece.ufl.edu

Abstract

Tracking radioactive sources in 3D can impact homeland security, airport/port surveillance and the military. Unfortunately, the radiological sensors with the highest SNR and the lowest price are unidirectional - i.e. they integrate radiation from a sphere of directions centered at the sensor. We combine such devices with commercially available depth sensors to break this directional ambiguity. We first introduce radiological sensing as an application area for the 3D vision community. Next, we propose a joint calibration algorithm for 3D sensors and unidirectional, or single cell*, radiological sensors. Finally, we show applications for tracking people carrying radiological sources.*

1. Introduction

Accurate detection and tracking of radioactive materials has many implications for world security, safety and health. First, any radioactive material could lead to bodily harm if misplaced or purposely transported undetected [8]. Second, such materials could be used in radiation dispersion devices (RDDs) which could have a massive economical and societal cost if detonated near a populous area. Lastly, special nuclear materials (SNM), such as uranium and plutonium could potentially be used in atomic weapons. The volume of SNMs needed for a atomic weapon is less than 1 litre (1000 cm^3), and poses a grave proliferation threat. Therefore the ability to detect and track nuclear materials is paramount. The seriousness of the situation is further underlined by considering the 2500 (reported) incidents of nuclear material incidents and trafficking have been reported in the IAEA Incident and trafficking database [1].

The typical tool used to detect nuclear material or nuclear activities are radiation detectors. These sense energy (neutrons, gamma radiation etc.) emitted from the radioactive sources. Like other energy sources, the intensity of these emitted radiations, and their detection, decreases with increase in distance. Low-cost single cell radiation detectors (on the order of $1000) do not have any angular resolution and detect sources all around the device. If correspondences for detections over time can be obtained, then these radiation detectors provide *both* the presence of radioactive sources and information relating to their 3D location.

This view of radioactive sensors as a 3D sensor for nuclear sources has made an impact in recent research that combines vision and radioactive detectors. In these efforts, visual sensors provide supporting information though satellite imagery, laser mapping and other modalities [21, 26, 25, 32, 3, 31]. However, the fusion of the data in these scenarios is enabled by expensive, custom built radioactive sensors with coded apertures that provide enhanced angular resolution. Such multi-pixel sensors capable of radiological "imaging" allow easy calibration, but have costs of upwards of $100,000. Additionally, they coded apertures decrease distance resolution due to the penetrability and diffusivity of emitted and transported radiation.

In this paper, we combine low-cost, uni-directional, single cell, "non-imaging" radiological sensors with commercially available depth sensors. We propose calibration algorithms and fusion strategies such that radiological source tracking for moving objects can be achieved at costs which are orders of magnitude lower that currently possible. The algorithms that we use are loosely related to near-lighting models in computer vision [30, 13], where depth cues are obtained by modeling the inverse square fall-off of light intensity from sources. In our case, we exploit the fall-off of radioactive strength with increase in distance.

Our contributions are:

- We introduce to the 3D vision community the potential for applications in the radiological domain. We survey existing work in the nuclear detection community and outline a variety of possible research directions. The key idea here is that radiological sensors can be another fruitful domain for 3D vision research.
- We propose a new calibration algorithm for unidirectional radiological sensors and commercially available depth sensors. Unlike all previous efforts, our calibration works with a uni-directional single-cell radiolog-

Table 1. Some basic properties of the four common types of ionizing radiation as compared to visible or IR light photons.

information carrier	energy[23]	mass[23]	thickness air to reduce intensity to half[18]	material needed to reduce by 90% [18]	detection mechanism [18]
light photons	few eV	0	$\sim$ km	$\sim 10^{-6}$ m Al	photo-absorption sensor
alpha	several MeV	$6.6{*}10^{-27}$ kg	$\sim$ cm	m	material (gas) ionization
beta	0 – 4 MeV	$9.9{*}10^{-31}$ kg	$\sim$ m	$\sim$ mm Al	material ionization
gamma	$\sim$ 1 MeV	0	$\sim$ 10's m	$\sim$ cm Pb	Compton scatter, photo-electric absorption
neutron	$\sim$ 1 MeV	$1.7{*}10^{-27}$ kg	$\sim$ 10's m	$\sim$ dm Concrete	elastic scatter & absorption on nuclei

ical sensor. We empirically analyze this algorithm's noise sensitively and demonstrate calibration results.

- Leveraging our calibration algorithm, we propose a new algorithm for tracking and detecting a single radiological source carried by one person in a group, by fusing radiological and depth sensor data.

1.1. Related Work

3D Vision and Radiological Fusion: Recent efforts in fusing LIDAR and radiological sensors focuses on static scenes [21, 26, 25] where the sensing gantry is rigidly constructed and no free form calibration is proposed. Other efforts use imaging [32] (non single cell detector) sensors created with coded apertures. These are used to average measurements and reduce noise through a frequency based approach similar to intrinsic image creation [2]. [3] using imaging to recover scene material properties, which provide a prior for estimating background radiation and compensating for this. [31] use a stereo system with a coded aperture to detect cars. We expect to replicate this type of performance at a fraction of the cost by using single cell detectors.

Sensor Fusion: Sensor fusion across multi-spectral, thermal, acoustic, sonar, LIDAR and other modes has been widely practiced in 3D vision [10, 28], and recent efforts using commercially available depth sensors have proved successful [16]. Data fusion of multi-sensor data for radiation detection have seen some interesting developments such as intelligent radiation sensor systems (IRSS) [9], which are based on larger numbers of distributed similar or identical radiation sensors coupled with position data for network capable to detect and locate radiation source. Statistical models of distributed sensors have also been investigated to couple with IRSS style systems [27]. For more exotic fusion of data one can consider a vast amount of different signatures and data sets available through different types of sensors. In the case of cargo scanning one such example is the fusion of data from radiation sensors and electromagnetic induction data [20]. While data fusion offers intriguing possible benefits, it is not always a clear benefit in the signal-to-noise ratio or multiple distributed sensors [19]. Further the way to perform the data fusion especially for the sake of localization can be done in a multitude of ways including but not limited to: deterministic solutions such as inverse-law inference [5], Maximum Likelihood Estimator [14], probabilistic solutions such as 2-dimensional least squares fitting [15], sequential probability testing[17], and Bayesian posterior estimation [22]. We present a geometric model for sensor fusion and analyze a few of its noise characteristics.

Near Lighting: Most computer vision techniques assume distant lighting, such as the sun or the sky. However, near lighting is present in indoor scenes, night scenes and underwater situations. In [7] a closed form scene geometry estimation is presented for vibrating near light sources. In [30] Helmholtz reciprocity was exploited from two dual stereo views to remove the effect of material properties on stereo matching. In all these efforts, the inverse square falloff from the light-source was used to obtain scene information. We exploit the fall-off from the radiological source to track the source in 3D, with the help of a depth sensor.

2. Background: Radiological Detectors as 3D Sensors

In contrast to the photons that are detected by 3D vision sensors, the two types of charged ionizing radiation (alpha and beta particles) lose energy and slow down in air, often to centimeter and meter ranges (see Table 1). Therefore we only consider uncharged radiation in this paper, such as neutrons and gamma rays, which have mean free paths on the order of 100-1000 m in air and enable fusion with vision sensors that operate on similar scales.

The key difference between light and uncharged radiation, one that offers an opportunity for interesting algorithms, is that neutrons and gamma rays have no notion of full opaqueness and can pass through clothing, lenses, humans and other materials. This opens up algorithms for detecting and tracking objects that vision sensors cannot see, such as illicit radiological material. Conversely, the materials used for shielding against radiological sensing can be bulky and opaque and may be easily tracked by a vision sensor with line-of-sight. Table 1 details some of the relevant particle and quanta information for radiation as well as near-visible-light photons. Note that while some types of radiation can be effectively shielded, others maintain relatively strong fluxes even after traveling through diverse materials.

2.1. Radiological Sensing and Scene Depths

In the case of detecting radiation the count rate is normally inversely dependent on the square of the distance,

$$D = \lambda(x, y, z) * e^{-\sigma R} * \frac{1}{R^2}. \quad (1)$$

Where the λ is a function of the size of the radiological sensor and its internal efficiency, normally referred to as intrinsic efficiency, (x, y, z) is the 3D location of the source and $R = \sqrt{x^2 + y^2 + z^2}$ is the radial distance from source to sensor.

The intrinsic efficiency can be considered to be a kind of "nuclear albedo". Intrinsic efficiency varies depending on what type of detector is used, as well as which type of radiation is detected in case the radiation detection sensor is capable of detecting multiple types of radiation. The aspect of the nuclear material being the source itself means that all other objects in the environment are "illuminated" or irradiated by the source. Most radiation will readily penetrate regular material, scatter in new directions or be absorbed. Thus if a radiation source is located near a larger object that object will in turn scatter some radiation that was initially emitted in a direction other than the direction of the radiation detector, this can add to the count rate that is observed. Typical examples of this would be when the source is located near a floor or wall. Additionally, even in the absence of large objects or boundaries in the scene there is still another weak dependence as a function of distance which is the scattered and absorbed radiation through the medium between the source and the radiation detector. This dependence is governed by the normally small parameter σ that depends on the medium (normally air).

Recovering the scene geometry (x, y, z) from radiological measurements D can be challenging, especially since λ can be scene dependent. Fortunately, in practice, the first two factors in Eq. (1) can be approximated as a slow varying function of radial distance $\lambda(R)$,

$$D = \lambda(R) * \frac{1}{R^2}. \quad (2)$$

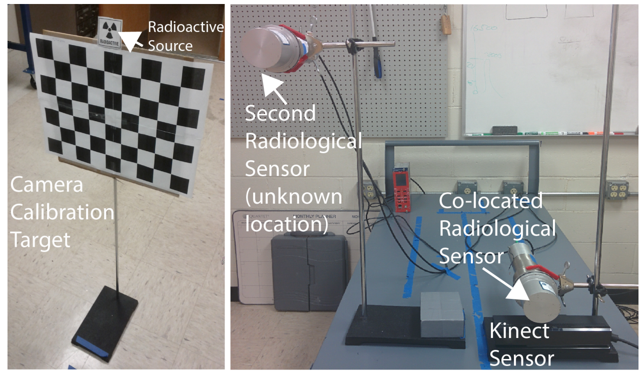

Figure 1. **A calibration target with a radiological source attached:** We attach a radiological source on a calibration target to simultaneously calibrate a single cell radiological sensor and a depth sensor. We also place a radiological sensor close to the depth sensor, as a form of approximate co-location. We combine traditional vision calibration [4] with radiological calibration to estimate the location of the second (or other multiple) radiological sensors with unknown location.

We will use this to track radiological sources in the last section. However, the radial distance is not useful without the sensor location. We will now propose how to estimate the location of both the vision and radiological sensor.

3. Calibration

We propose a method to simultaneously calibrate a depth sensor and a radiological sensor. The key idea is to attach a radiological beacon or source to the commonly used checkerboard pattern as in Fig 1. The checkerboard pattern allows bundle-adjustment based geometric calibration [29], while the depth locations are used to calibrate the radiological sensor. Since camera calibration is well understood, we focus on the latter portion of the calibration.

A single cell radiological sensor consists of a chamber where neutrons or gamma rays are captured and release photons. These photons are measured by a single pixel camera. Therefore the model for the radiological sensor that we use is simply a point location in space, (S_x, S_y, S_z). Since the neutrons and gamma rays may scatter inside the chamber, this model is approximate.

After processing the radiological counts, we can model the fall-off measurement for any particular location i of the calibration pattern as,

$$(B_x^i - S_x)^2 + (B_y^i - S_y)^2 + (B_z^i - S_z)^2 = R^2 = \frac{\lambda(R)}{D}. \quad (3)$$

where $B^i = (B_x^i, B_y^i, B_z^i)$ is the location of the radiological source at the ith location of the calibration target. We utilize all the calibration pattern images to first calibrate the depth sensor using traditional camera calibration [4]. Then,

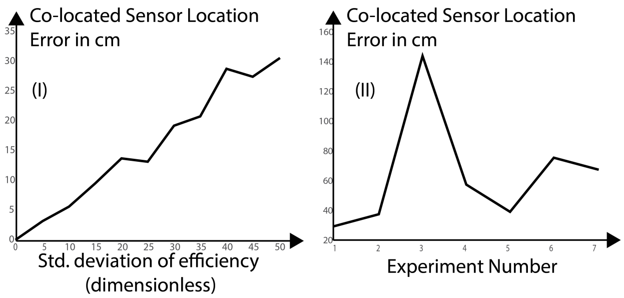

Figure 2. **Noise:** In (I) we study how the error in our algorithm increases with increase in estimates of the intrinsic efficiency $\lambda(R)$. We pick a scenario where the groundtruth location and groundtruth intrinsic efficiencies are known, and add noise to the intrinsic efficiencies. These increase the error linearly. In (II) we show how our assumption of radially dependent intrinsic efficiency $\lambda(R)$ vs. the reality of spatially dependent intrinsic efficiency $\lambda(x, y, z)$ affects our analysis. We reconstruct the co-located sensor (whose ground truth location is known) with the parabolic fit to $\lambda(R)$, showing significant errors that can be caused by our model.

we utilize the depth sensor's projection matrix, along with the measured depth, to obtain B^i for every location of the calibration pattern. We assume that the beacon can be easily visually distinguished in every image - this is easily possible during this one-time calibration step.

We consider two cases when proposing our calibration algorithm. In the first, we assume a situation where the intrinsic efficiency λ can be assumed to be near constant. This may happen if the source strength is high and if the scene geometry is relatively open and free of obstacles. In the second step, we relax this assumption.

Constant Source Strength: In Eqn. 3 we replace $\lambda(R)$ with λ. The equation appears non-linear in terms of the four unknowns (S_x, S_y, S_z, λ) , but we perform a numerical approximation of the first derivative, to make its solution linear. Consider pairs of equations obtained from, say, locations of the calibration pattern at i and j. Subtracting two such equations eliminates the non-linear terms,

$$(2B_x^i - 2B_x^j)S_x + (2B_y^i - 2B_y^j)S_y \quad (4)$$

$$+(2B_z^i - 2B_z^j)S_z + \left(\frac{1}{D_i} - \frac{1}{D_j}\right)\lambda = \quad (5)$$

$$(B_x^i)^2 - (B_x^j)^2 + (B_y^i)^2 - (B_y^j)^2 + (B_z^i)^2 - (B_z^j)^2. \quad (6)$$

If there are n calibration pattern positions, we obtain $\binom{n}{2}$ such equations. We build a linear equation $\mathbf{Ax} = \mathbf{b}$, where $\mathbf{x}$ are the unknown variables (S_x, S_y, S_z, λ), the rows of $\mathbf{A}$ are the known coefficients in Eq. 4 and $\mathbf{b}$ are the R.H.S of Eq. 4, given by the depth sensor.

The above equation essentially finds the center point that explains the radiological fall-off as the calibration pattern is moved around. Geometrically, this is equivalent to finding the intersection of multiple spheres in a least-square sense, each of which are centered at the radiological source. The intersection of the spheres is the desired, unknown, sensor location. Similar systems of equations have been solved for near light photometric stereo [24] in the vision community. Like those equations, we require at least 4 measurements and we face the same degenerate cases that occur when $\mathbf{A}$ does not have full rank. This include situations that are well understood in photometric stereo, such as when the light-sources lie along a line or a plane. In practice, we have noticed that the randomly selected locations used when moving a calibration pattern around a camera avoid these cases, and the matrix is usually full rank and well conditioned.

Spatially-varying Source Strength: The intrinsic efficiency's dependence on distance $\lambda(R)$ becomes difficult to solve because this dependence is created by reflections and scattering in scene geometry. Modeling such radiological scattering through Monte Carlo based simulations requires scene properties, which are unknown to us.

To address this challenge, we propose a non-linear optimization with two characteristics. The first takes advantage of the dependence of the intrinsic efficiency $\lambda(R)$ on the source location (S_x, S_y, S_z), since $R = \sqrt{S_x^2 + S_y^2 + S_z^2}$. The second approximates the radial intrinsic efficiency model $\lambda(R)$ from measurements given by an additional single cell radiological sensor co-located with the depth sensor, as shown in Fig. 1. This sensor is assumed to be at the origin ($S_x = 0, S_y = 0, S_z = 0$), and (with the depth sensor) allows direct measurement samples of the intrinsic efficiency $\lambda(R)$ in Eq. 4. We fit a parabolic model to the $\lambda(R)$ samples, essentially learning the spatially varying source strength for this particular scene.

The optimization then proceeds as follows; given a candidate sensor location (S_x, S_y, S_z), we obtain the intrinsic efficiency $\lambda(R)$ from the parabolic model. Eq. 4 and the intrinsic efficiency can be used to calculate the estimated sensor locations $(\hat{S}_x, \hat{S}_y, \hat{S}_z)$ and the error $E = \sqrt{(\hat{S}_x - S_x)^2 + (\hat{S}_y - S_y)^2 + (\hat{S}_z - S_z)^2}$ can be calculated. We minimize this error to find the best candidate, using a grid search technique where the sensor location candidates occur in a fixed volume region around the origin.

This strategy has two assumptions. The first is that the geometry of the room will not change significantly after the calibration procedure. The second is that the estimated $\lambda(R)$ does not change significantly with the change in viewpoint of the radiological source. This second assumption is not true for a distant radiological source.

Finally emphasize the importance of calibration the second radiological sensor, since the co-located vision and radiological sensor by themselves are not optimal for many scenarios. For example, in radiological tracking in hallways, a vision sensor must be placed at one end of the cor-

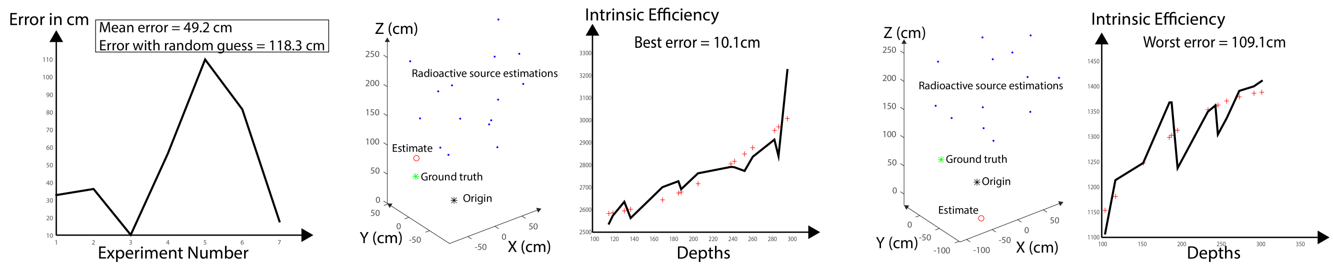

(I) Error in cm for seven calibration experiments

(II) 3D plot for best calibration result with estimated intrinsic efficiency

(III) 3D plot for worst calibration result with estimated intrinsic effiiciency

Figure 3. **Result:** We performed seven experiments, moving the radiological sensor to different positions and estimating its location using the Kinect depth sensor and the co-located additional radiological source. We measured the ground truth location of the sensor and compared the error in (I). Our average error is 49.2cm, and compared favorably with randomly guessing the location of the sensor in the grid search volume around the origin of the system. In (II) and (III) we show 3D views and the parabolic fit to the intrinsic efficiency $\lambda(R)$ for the best and worst results from (I). Both (II) and (II) show the estimated radiological sensor locations - we center spheres on each of these locations with radii determined by the intrinsic efficiency and the radioactive count, and use these intersecting spheres to estimate the sensor location. Note that the parabolic fit for the intrinsic efficiency is tighter when the result is better. Although we use our model for intrinsic efficiency as is, these graphs show promise to reduce the error further in the future with a better model for intrinsic efficiency.

ridor due to field-of-view restrictions, but a 360 degree sensitive radiological sensor can be placed at the center of the hallway, which allows better detection sensitivity. Our calibration can enable such a system.

3.1. Calibration Results

We demonstrate our calibration algorithm on a real combination of radiological sensors and a depth camera. We use the Microsoft Kinect V2, which is a 512×424 resolution depth camera that uses infra-red time-of-flight for scene recovery. The radiological detector is based on the well-characterized organic liquid EJ-309 compound [11, 12] with a high flashpoint and low chemical toxicity compared to many other detector liquids. The liquid is encapsulated in an alumina cell. It has 75% light output compared to the reference material Anthracene, a wavelength of maximum emission of 424 nm, and a time constant of fast decay of 3.5 ns. The detector used was cylindrical in shape, and of identical dimensions (7.36-by-7.36 cm). The scintillation light was absorbed by a photomultiplier tube (ET-Enterprises 9821B), and then converted into an electronic signal with a high gain. The photomultiplier was consistently powered at 1690 V by a remotely controlled power system, manufactured by CAEN. The voltage was set as to maintain consistent detector calibration and radiation response. An additional second identical detector was used at the same time to test the data-fusion calibration algorithms with. The data acquisition system was composed of a 14 bits, 250 MHz, 16-channel digitizer in the form of a Struck SIS3316 unit. Where each input channel has a significant buffer memory to acquire large amounts of pulse data and send it to a data acquisition computer for storage and analysis. The radiological detection system is sensitive to both gamma-rays and fast neutrons, and the data analysis provides details on which pulse was generated by which particle type, enabling two separate count rates if desired. This could be an advantage in cases of sources being shielded by some material. The nature of gamma-ray and neutron interactions are such that a single shielding material is normally only able to stop one of the two types of radiation efficiently. Lead (Pb) and water are efficient shielding materials for gamma-rays and neutrons respectively.

Noise analysis of calibration algorithm: We performed 7 experiments, moving the radiological sensor to a variety of locations around the depth camera and using our calibration process to recover its location in 3D. As shown in Fig. 1, we used an additional radiological sensor placed at the Kinect to estimate the intrinsic efficiency. The calibration target used in Fig 1 fixes the Kinect to be at the origin, with its intrinsic camera parameters estimated by the process [4]. All our measurements are in centimeters (cm) and we searched for candidate locations using a grid search technique in a $100 \times 100 \times 100$ volume around the origin.

We will first explain the noise characteristics of our algorithm through empirical simulations. We performed experiments shown in Fig. 2 (I), where we analyzed the error in recovering the position of the co-located radiological sensor, instead of the second, unknown radiological sensor. This has the advantage of known ground truth (location at the origin, since the sensor is co-located with the Kinect depth sensor) and known intrinsic efficiency $\lambda(R)$, since R is known, again from the Kinect sensor. With no noise, we recover the system origin with zero error, as in the first entry of Fig. 2 (I). As gaussian noise increases, the error increases linearly. This means that scenes that do not obey our assumption of constant intrinsic efficiency will cause linearly increasing calibration errors.

In the second experiment, shown in Fig. 2 (II), we show

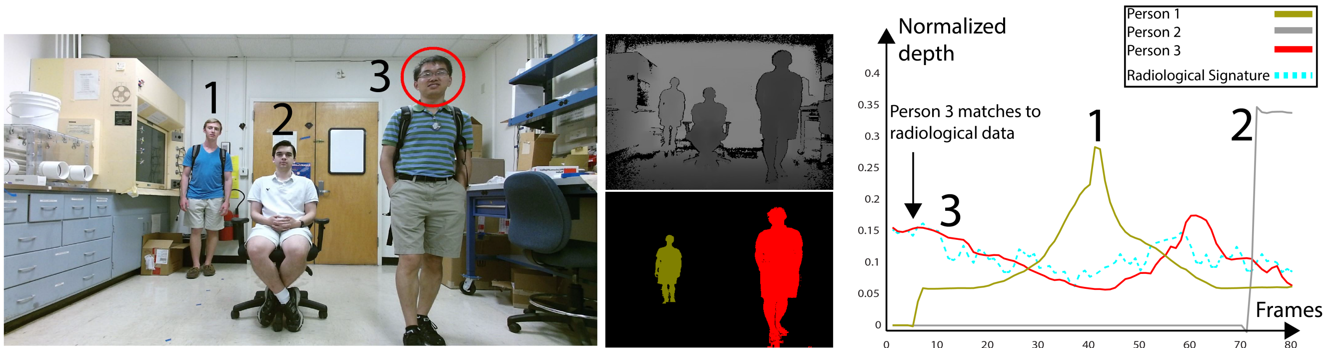

(Ia) Frames from Microsoft Kinect showing the depth map and native tracking, with the person carrying the radioactive source highlighted

(Ib) Normalized depth trajectories compared with radiological data

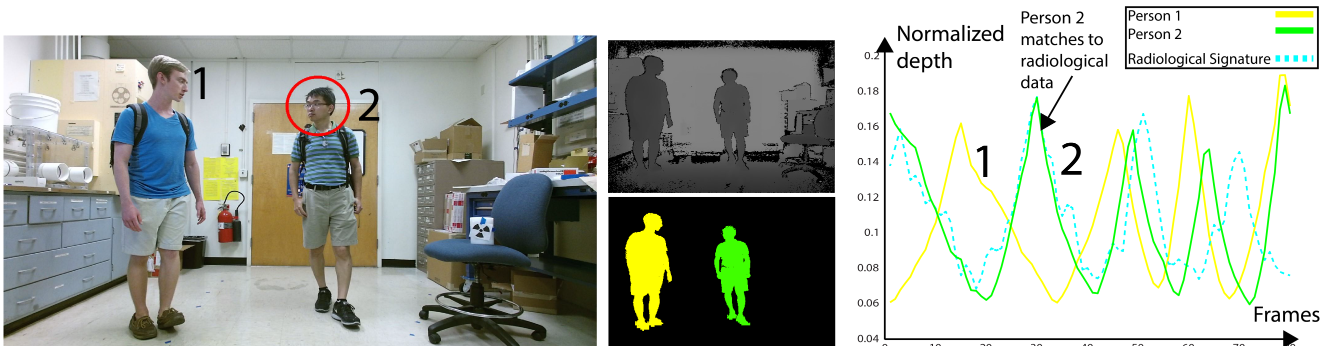

(IIa) Frames from Microsoft Kinect showing the depth map and native tracking, with the person carrying the radioactive source highlighted

(Ib) Normalized depth trajectories compared with radiological data

Figure 4. **Tracking a single radiological source among multiple objects:** We placed a radiological source in the backpack of one of the people moving around a laboratory scene. We tracked the people using the native Microsoft Kinect V2 tracker (Ia and IIa). We utilized our calibration algorithm to obtain the location of the sensor placed away from the Kinect. In this case our error was around 20cm from the ground truth. Using this calibration result, we recovered the radiological source's trajectory, plotted in Ib and IIb as a dashed line. We compared this with the trajectories from the Kinect depth tracking and correlated the best match using normalized dot-product distance. The selected person is highlighted with a red circle. In these two experiments, this was the person carrying the radiological source.

how our assumption of radially dependent intrinsic efficiency $\lambda(R)$ vs. the reality of spatially dependent intrinsic efficiency $\lambda(x, y, z)$ affects our analysis. We recover the location of the co-located sensor (ground truth at the origin) using not the ground truth intrinsic efficiency values but the values obtained by fitting a parabola (in the least squares sense) to the data. In other words, we recover the location of the co-located sensor when the intrinsic efficiencies have residual errors due to our model. The large errors show that our model and assumptions can be off-target, depending on the scene geometry and its material properties. Addressing this is one of our goals in the future, and we present the results of the calibration using this imperfect model.

Calibration results: The results of recovering the locations of the radiological sensor over seven different experiments are shown in Fig. 3. The ground truth was obtained with careful manual measurements of the location of the radiological sensor. We are able to obtain the location of the source with an average error of 49.2cm. While this may seem prohibitively large by 3D vision standards, we note that the radiological sensor is a 7.36-by-7.36 cm cylinder, and that the $\lambda(R)$ fit may be noisy as shown by the parabolic fit in Fig. 3. Further, randomly guessing the location in the grid search space of $100 \times 100 \times 100$ with a uniform distribution of sensors gives an error of 118.3cm, which demonstrates that our calibration algorithm provides a factor of 2 increase in accuracy. This is the first time that a single unidirectional radiological source and a depth sensor have been calibrated, and there are no competing algorithms to compare against.

4. Application: Tracking a Single Radiological Source

We address the problem of tracking a single radiological source, that is hidden amongst multiple moving targets. Each target was a person walking around a laboratory environment with a backpack. The radiological source was placed in one of the person's backpack. We assume that the targets are visible to the vision sensor, which is performing visual tracking of salient objects in the scene.

We performed two experiments, as shown in Fig. 4, each lasting approximately one minute. We utilized our calibration algorithm to obtain the location of the sensor placed away from the Kinect. The groundtruth sensor location was $(-57cm, -59cm, 0cm)$ and the calibration estimate was $(-73.49cm, -38.63cm, -9.5cm)$, showing a 20cm error.

We use the native Microsoft Kinect people tracker, that can detect two moving persons and up to six static people in the scene. The native Kinect calibration library allows us to convert this tracking into a trajectory of the person's mean depth in 3D. While the person's 3D location is not the same as the exact 3D location of the radiological source on the person, it proved to be a robust approximation in practice. In Fig. 4 we compare these trajectories to the trajectory obtained from the radiological sensor. This radiological trajectory is based on the radioactive sensor counts, the intrinsic efficiency model $\lambda(R)$ learned from the co-located source and the calibration of the radiological location.

In Fig. 4 we plot the normalized candidate trajectories and the radiological source trajectory. We used the dot-product metric with these normalized trajectories and were able to localize the depth sensor in the backpack of the person correctly and in both experiments we were able to highlight this person in the video frames, as shown in the figure.

5. Limitations and Discussion

This is the first effort to fuse the results from a single unidirectional radiological source and a commercially available depth sensor. The impact of this work can be low-cost 3D radiological tracking that can be widely used in airports, commercial areas and battlefield scenarios with positive security benefits. However, we point out a few limitations that we hope to address in future work:

Radial efficiency model: The noise analysis shown in this paper demonstrates that a radial assumption for the "efficiency" parameter, λ, allows noisy recovery of the radiological sensor location. To improve this model, we must analyze the statistical variation of intrinsic efficiency across a large range of radioactive sources and scene geometry/material combinations, with the goal of learning a prior to improve the model. The fact that the Kinect provides a scene depth estimate could be used for a first order estimation of the effect of scattering on the intrinsic efficiency.

Single source: Our algorithm assumes that the multiple person trajectories can easily be mapped to a single radiological trajectory. With multiple source, perhaps of different radiological materials, or even a volumetric source such as liquid or gas, these assumptions must change.

Static source: Our algorithm can only match the radiological source to closest object trajectory. If the source is static, no moving object's trajectory will match the target, as shown in Fig. 5. Further, every static object in the scene will match to the radiological trajectory, which results in an ambiguity. In presence of a very strong stationary scene source this adds a significant time-constant background which is subject to calibration background subtraction on the radiological sensor elevating the noise-level in that scenario.

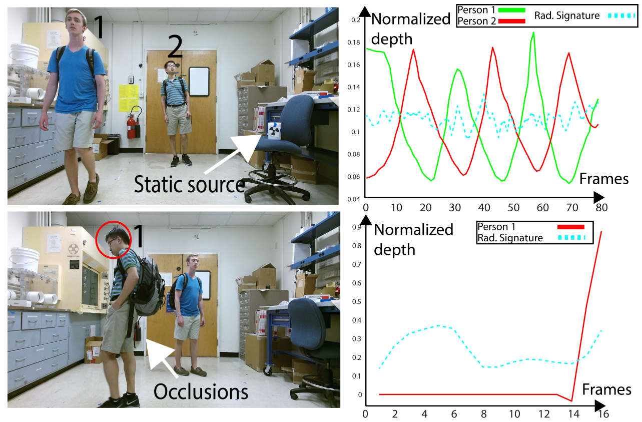

Figure 5. **Limitations of our approach:** Our approach cannot currently handle static scenes (top). We also are using the native Microsoft Kinect tracker (bottom) that results in problems with occlusions. In the future, we can use more sophisticated people tracking algorithms (such as [6]) to improve the results in these scenarios.

Occlusions: We also are using the native Microsoft Kinect tracker that results in problems with occlusions. In the future, we can use more sophisticated people tracking algorithms (such as [6]) to improve the results in these scenarios. In Fig. 5 we show tracking when the people did occlude each other. We were only able to localize the source on the person in a few frames.

6. Acknowledgements

This material is based upon work supported by the U.S. Department of Homeland Security under Grant Award Number, 2014-DN-077-ARI083-01. The views and conclusions contained in this document are those of the authors and should not be interpreted as necessarily representing the official policies, either expressed or implied, of the U.S. Department of Homeland Security.

References

[1] Application of nuclear forensics in combating illicit trafficking of nuclear and other radioactive material. In *IAEA TECDOC Series 1730*, 2014.

[2] H. Barrow and J. Tenenbaum. Computer vision systems. *Computer vision systems*, page 2, 1978.

[3] B. Bernacki, J. Schweppe, S. Stave, D. Jordan, J. Kulisek, T. Stewart, and C. Seifert. Estimating radiological background using imaging spectroscopy. In *SPIE Defense+ Security*, pages 90880L–90880L. International Society for Optics and Photonics, 2014.

[4] J.-Y. Bouguet. Camera calibration toolbox for matlab. 2004.

[5] J.-C. Chin, D. K. Yau, N. S. Rao, Y. Yang, C. Y. Ma, and M. Shankar. Accurate localization of low-level radioactive source under noise and measurement errors. In *Proceedings of the 6th ACM Conference on Embedded Network Sensor Systems*, SenSys '08, pages 183–196, New York, NY, USA, 2008. ACM.

[6] W. Choi, C. Pantofaru, and S. Savarese. Detecting and tracking people using an rgb-d camera via multiple detector fusion. In *Computer Vision Workshops (ICCV Workshops), 2011 IEEE International Conference on*, pages 1076–1083. IEEE, 2011.

[7] J. J. Clark. Active photometric stereo. In *Computer Vision and Pattern Recognition, 1992. Proceedings CVPR'92., 1992 IEEE Computer Society Conference on*, pages 29–34. IEEE, 1992.

[8] T. B. Cochran and M. G. McKinzie. Detecting nuclear smuggling. *Scientific American*, 298(april):98 – 104, 2008.

[9] D. Cooper, R. Ledoux, K. Kamieniecki, S. Korbly, J. Thompson, J. Batcheler, S. Chowdhury, N. Roza, J. Costales, and V. Aiyawar. Intelligent radiation sensor system (irss) advanced technology demonstrator (atd). In *Homeland Security (HST), 2012 IEEE Conference on Technologies for*, pages 511–516, Nov 2012.

[10] J. L. Crowley. Principles and techniques for sensor data fusion. In *Multisensor Fusion for Computer Vision*, pages 15–36. Springer, 1993.

[11] S. T. . Eljen Technology, P. O. Box 870. `http://www.eljentechnology.com/images/stories/Data_Sheets/Liquid_Scintillators/EJ309datasheet.pdf`. 2012.

[12] A. Enqvist, C. C. Lawrence, B. M. Wieger, S. A. Pozzi, and T. N. Massey. Neutron light output response and resolution functions in ej-309 liquid scintillation detectors. *Nuclear Instruments and Methods in Physics Research Section A: Accelerators, Spectrometers, Detectors and Associated Equipment*, 715(0):79 – 86, 2013.

[13] D. Frolova, D. Simakov, and R. Basri. Accuracy of spherical harmonic approximations for images of lambertian objects under far and near lighting. In *Computer Vision-ECCV 2004*, pages 574–587. Springer, 2004.

[14] A. Gunatilaka, B. Ristic, and R. Gailis. On localisation of a radiological point source. In *Information, Decision and Control, 2007. IDC '07*, pages 236–241, Feb 2007.

[15] J. W. Howse, L. O. Ticknor, and K. R. Muske. Least squares estimation techniques for position tracking of radioactive sources. *Automatica*, 37(11):1727 – 1737, 2001.

[16] S. Izadi, D. Kim, O. Hilliges, D. Molyneaux, R. Newcombe, P. Kohli, J. Shotton, S. Hodges, D. Freeman, A. Davison, et al. Kinectfusion: real-time 3d reconstruction and interaction using a moving depth camera. In *Proceedings of the 24th annual ACM symposium on User interface software and technology*, pages 559–568. ACM, 2011.

[17] K. Jarman, L. Smith, D. Carlson, and D. Anderson. Sequential probability ratio test for long-term radiation monitoring. In *Nuclear Science Symposium Conference Record, 2003 IEEE*, volume 2, pages 1458–1462 Vol.2, Oct 2003.

[18] G. Knoll. *Radiation Detection and Measurement*. John Wiley & Sons, 2010.

[19] A. Liu, J. Bunn, and K. Chandy. An analysis of data fusion for radiation detection and localization. In *Information Fusion (FUSION), 2010 13th Conference on*, pages 1–8, July 2010.

[20] Z. Long, W. Wei, A. Turlapaty, Q. Du, and N. Younan. Fusion of radiation and electromagnetic induction data for buried radioactive target detection and characterization. *Nuclear Science, IEEE Transactions on*, 60(2):1126–1133, April 2013.

[21] L. Mihailescu, K. Vetter, and D. Chivers. Standoff 3d gamma-ray imaging. *Nuclear Science, IEEE Transactions on*, 56(2):479–486, 2009.

[22] M. Morelande and A. Skvortsov. Radiation field estimation using a gaussian mixture. In *Information Fusion, 2009. FUSION '09. 12th International Conference on*, pages 2247–2254, July 2009.

[23] C. Nordling and J. Osterman. *Physics Handbook*. Studentlitteratur, 8th edition, 2006.

[24] T. Papadhimitri and P. Favaro. Uncalibrated near-light photometric stereo. *BMVC*, 2014.

[25] A. C. Raffo-Caiado, K.-P. Ziock, J. Hayward, S. Smith, J. Bogard, and C. B. Boehnen. Combining measurements with three-dimensional laser scanning system and coded-aperture gamma-ray imaging systems for international safeguards applications. In *2010 IAEA Symposium on International Safeguards*, pages 1–5, 2010.

[26] A. C. Raffo-Caiado, K.-P. Ziock, J. Hayward, S. Smith, A. Solodov, L. Mihailescu, K. Vetter, A. Dougan, M. Burks, J. G. Gonçalves, et al. Investigation of combined measurements with three-dimensional design information verification system and gamma-ray imaging systems for international safeguards applications. In *Proceedings 50th INMM Annual Meeting*, pages 12–16, 2009.

[27] A. Sundaresan, P. Varshney, and N. Rao. Distributed detection of a nuclear radioactive source using fusion of correlated decisions. In *Information Fusion, 2007 10th International Conference on*, pages 1–7, July 2007.

[28] M. Ye, Y. Zhang, R. Yang, and D. Manocha. 3d reconstruction in the presence of glasses by acoustic and stereo fusion. In *Proceedings of the IEEE Conference on Computer Vision and Pattern Recognition*, pages 4885–4893, 2015.

[29] Z. Zhang. A flexible new technique for camera calibration. *Pattern Analysis and Machine Intelligence, IEEE Transactions on*, 22(11):1330–1334, 2000.

[30] T. E. Zickler, P. N. Belhumeur, and D. J. Kriegman. Helmholtz stereopsis: Exploiting reciprocity for surface reconstruction. *International Journal of Computer Vision*, 49(2-3):215–227, 2002.

[31] K.-P. Ziock, E. C. Bradley, A. Cheriyadat, M. Cunningham, L. Fabris, C. Fitzgerald, J. Goddard, D. E. Hornback, R. A. Kerekes, T. P. Karnowski, et al. Performance of the roadside tracker portal-less portal monitor. *Nuclear Science, IEEE Transactions on*, 60(3):2237–2246, 2013.

[32] K. P. Ziock, W. W. Craig, L. Fabris, R. C. Lanza, S. Gallagher, B. K. Horn, and N. W. Madden. Large area imaging detector for long-range, passive detection of fissile material. *Nuclear Science, IEEE Transactions on*, 51(5):2238–2244, 2004.